

# RSC Advances



This is an *Accepted Manuscript*, which has been through the Royal Society of Chemistry peer review process and has been accepted for publication.

*Accepted Manuscripts* are published online shortly after acceptance, before technical editing, formatting and proof reading. Using this free service, authors can make their results available to the community, in citable form, before we publish the edited article. This *Accepted Manuscript* will be replaced by the edited, formatted and paginated article as soon as this is available.

You can find more information about *Accepted Manuscripts* in the [Information for Authors](#).

Please note that technical editing may introduce minor changes to the text and/or graphics, which may alter content. The journal's standard [Terms & Conditions](#) and the [Ethical guidelines](#) still apply. In no event shall the Royal Society of Chemistry be held responsible for any errors or omissions in this *Accepted Manuscript* or any consequences arising from the use of any information it contains.



## Graphitic-C<sub>3</sub>N<sub>4</sub>-hybridized Ag<sub>3</sub>PO<sub>4</sub> tetrahedron with reactive {111} facets to enhance the visible-light photocatalytic activity

Received 00th September 2015,  
Accepted 00th September 2015

DOI: 10.1039/x0xx00000x

www.rsc.org/

Chunni Tang,<sup>ab</sup> Enzhou Liu,<sup>a</sup> Jun Fan,<sup>\*a</sup> Xiaoyun Hu,<sup>c</sup> Yongning Ma<sup>a</sup> and Jun Wan<sup>a</sup>

Graphitic-C<sub>3</sub>N<sub>4</sub>-hybridized Ag<sub>3</sub>PO<sub>4</sub> tetrahedron with reactive {111} facets was prepared through a facile solvent evaporation method and applied for the photocatalytic degradation of methyl blue (MB) in aqueous solution and removal of NO at the indoor air level under visible light irradiation (>400 nm). On top of the superior photocatalytic performance of highly reactive {111} facets of tetrahedral Ag<sub>3</sub>PO<sub>4</sub>, the hybridization with g-C<sub>3</sub>N<sub>4</sub> was confirmed to further improve the photocatalytic activity, and the content of g-C<sub>3</sub>N<sub>4</sub> had a great influence on the photocatalytic activity. The photocatalytic activity enhancement of g-C<sub>3</sub>N<sub>4</sub>/Ag<sub>3</sub>PO<sub>4</sub> {111} hybrid photocatalysts could be ascribed to the efficient separation of electron-hole pairs through a Z-scheme system composed of Ag<sub>3</sub>PO<sub>4</sub>, Ag and g-C<sub>3</sub>N<sub>4</sub>, in which Ag particles acted as the charge separation center. Furthermore, h<sup>+</sup> and O<sub>2</sub><sup>•-</sup> played the major roles in the photocatalysis process. This work suggested that the synthesized g-C<sub>3</sub>N<sub>4</sub>/Ag<sub>3</sub>PO<sub>4</sub> {111} hybrid would be a promising visible light driven photocatalytic material for environmental remediation.

### 1 Introduction

The growing concerns about environmental pollution and energy crises have attracted extensive research on solar energy utilization. Semiconductor photocatalysis technology is believed to be a promising clean, low-cost, and environmentally friendly approach to cope with these crises [1,2]. Unfortunately, TiO<sub>2</sub> as the most widely employed semiconductor photocatalyst is only active under UV light irradiation (less than 5% of solar light). Therefore, the development of efficient visible light driven photocatalysts is a major challenge in this field. Recently, silver orthophosphate (Ag<sub>3</sub>PO<sub>4</sub>) has been reported as an active visible light driven photocatalyst for decolorization of organic pollutants and water photooxidation, and the photocatalytic performance of Ag<sub>3</sub>PO<sub>4</sub> is significantly higher than that of currently known visible light photocatalysts, such as TiO<sub>2-x</sub>N<sub>x</sub>, BiVO<sub>4</sub> and WO<sub>3</sub> [3]. Moreover, the photocatalytic activity of Ag<sub>3</sub>PO<sub>4</sub> can be further improved through the preparation on the morphology control, surface modification and element doping [4-8]. In addition, incorporation with other semiconductors (such as, TiO<sub>2</sub>, SnO<sub>2</sub>, ZnO, CeO<sub>2</sub>, Fe<sub>2</sub>O<sub>3</sub>, Bi<sub>2</sub>WO<sub>6</sub>, BiPO<sub>4</sub>, BiOI, WO<sub>3</sub>, oxidized grapheme, graphene, carbon nanotubes, etc.) is one of the effective methods because they can enhance the photogenerated charges separation [9-20].

A novel metal-free photocatalyst, named graphitic carbon nitride (g-C<sub>3</sub>N<sub>4</sub>) with layered structure similar to graphene is recognized as a promising candidate for photodegradation of organic pollutants and photocatalytic hydrogen evolution under visible-light irradiation due

to its remarkable structure, mechanical and electronic properties. The two-dimensional planar structure with  $\pi$ -conjugated system benefits the transport of charge carriers, and its high nitrogen content enable g-C<sub>3</sub>N<sub>4</sub> to provide more active reaction sites. Therefore, g-C<sub>3</sub>N<sub>4</sub> is widely used to couple with other semiconductor photocatalysts for enhancement of their photocatalytic activity, such as, TiO<sub>2</sub>, SiO<sub>2</sub>, ZnO, Al<sub>2</sub>O<sub>3</sub>, WO<sub>3</sub>, BiVO<sub>4</sub>, Ag<sub>2</sub>CO<sub>3</sub>, Ag<sub>3</sub>VO<sub>4</sub>, Bi<sub>2</sub>MoO<sub>6</sub>, In<sub>2</sub>O<sub>3</sub> and so on [21-30]. Currently, a few studies have been focused on combining g-C<sub>3</sub>N<sub>4</sub> with Ag<sub>3</sub>PO<sub>4</sub>. Zhang et al [31] used the ion-impregnating method to synthesis graphitic carbon nitride/silver phosphate (g-C<sub>3</sub>N<sub>4</sub>/Ag<sub>3</sub>PO<sub>4</sub>) bulk heterojunction, and it showed enhanced photocatalytic activity for decolorization of RhB. Santosh Kumar et al [32] developed a facile and reproducible template free in situ precipitation method for the synthesis of Ag<sub>3</sub>PO<sub>4</sub> nanoparticles on the surface of a g-C<sub>3</sub>N<sub>4</sub> photocatalyst at room temperature with improved photocatalytic performance. Katsumata et al [33] used a facile in situ precipitation method to prepare g-C<sub>3</sub>N<sub>4</sub>/Ag<sub>3</sub>PO<sub>4</sub> which displayed the higher photocatalytic activity than pure g-C<sub>3</sub>N<sub>4</sub> and Ag<sub>3</sub>PO<sub>4</sub> for the decolorization of methyl orange (MO).

Furthermore, the synthesis of crystals with highly reactive facets has sparked cosmic research interest because crystals usually exhibit fascinating surface-dependent properties. For Ag<sub>3</sub>PO<sub>4</sub>, evidenced by theoretical and experimental studies, the {111} facets of Ag<sub>3</sub>PO<sub>4</sub> are the most reactive facets among the {111}, {110} and {100} facets due to their highest surface energy [34]. The order of the average surface energies of Ag<sub>3</sub>PO<sub>4</sub> reported in the literature is 1.65 J m<sup>-2</sup> for {111} > 1.31 J m<sup>-2</sup> for {110} > 1.10 J m<sup>-2</sup> for {100} [35]. In consideration of this, we proposed that combining two strategies (exposed facets control and hybridization) to improve photocatalysis efficiency of Ag<sub>3</sub>PO<sub>4</sub> together. Therefore, g-C<sub>3</sub>N<sub>4</sub> hybridized Ag<sub>3</sub>PO<sub>4</sub> with reactive {111} facets photocatalyst is expected to

<sup>a</sup> School of Chemical Engineering, Northwest University, Xi'an 710069, PR China.  
E-mail: fanjun@nwu.edu.cn

<sup>b</sup> School of Chemical Engineering, Shaanxi Institute of Technology, Xi'an 710300, PR China Address here.

<sup>c</sup> School of Physics, Northwest University, Xi'an 710069, PR China

† Electronic Supplementary Information (ESI) available. See DOI: 10.1039/x0xx00000x

display excellent photocatalytic performance under visible light irradiation. To the best of our knowledge, g-C<sub>3</sub>N<sub>4</sub>/Ag<sub>3</sub>PO<sub>4</sub> {111} hybrid has not been reported in literatures so far. Furthermore, no one has ever reported the use of g-C<sub>3</sub>N<sub>4</sub>/Ag<sub>3</sub>PO<sub>4</sub> photocatalyst for the photocatalytic degradation of gaseous nitrogen monoxide (NO) thus far. Therefore, another significance of our work is that the newly developed photocatalyst is for the first time applied to photocatalytic NO removal, which would expand the research and application of g-C<sub>3</sub>N<sub>4</sub>/Ag<sub>3</sub>PO<sub>4</sub> materials.

In this paper, we developed a novel photocatalyst, g-C<sub>3</sub>N<sub>4</sub>/Ag<sub>3</sub>PO<sub>4</sub> {111} hybrid, via a solvent evaporation process. The photocatalytic performance was evaluated by photodegradation of methyl blue (MB) in aqueous solution and removal of NO at the indoor air level under visible light irradiation (>400 nm). The effect of the ratio of g-C<sub>3</sub>N<sub>4</sub> and Ag<sub>3</sub>PO<sub>4</sub> on photocatalytic activity was also investigated. In addition, the enhancement mechanism of the photocatalytic activity of g-C<sub>3</sub>N<sub>4</sub>/Ag<sub>3</sub>PO<sub>4</sub> {111} was also discussed.

## 2 Experimental

### 2.1 Preparation of few-layer g-C<sub>3</sub>N<sub>4</sub>

The few-layer g-C<sub>3</sub>N<sub>4</sub> was prepared by polymerization and chemical exfoliation method. Typically, melamine (C<sub>3</sub>H<sub>6</sub>N<sub>6</sub>) was put into a crucible, and then heated at 600 °C for 3 h. After the product cooled to room temperature, the resultant yellow powder was then collected and ground into a powder. Subsequently, as-prepared powder was treated with acetic acid (HAc) for chemical exfoliation. Finally, the sample of acid treatment was dispersed into ethanol, and then executed with ultrasonic-processing continuously for about 4 hours. The initial formed suspension was then centrifuged to remove the residual unexfoliated g-C<sub>3</sub>N<sub>4</sub> and the centrifugal liquid was obtained for further use.

### 2.2 Preparation of g-C<sub>3</sub>N<sub>4</sub>/Ag<sub>3</sub>PO<sub>4</sub> {111} hybrid

Tetrahedral Ag<sub>3</sub>PO<sub>4</sub> microcrystals (TE Ag<sub>3</sub>PO<sub>4</sub>) with exposed {111} facets were hybridized with g-C<sub>3</sub>N<sub>4</sub> through a simple two-step route. In a typical process, 0.17 g silver nitrate (AgNO<sub>3</sub>) ethanol solution was slowly dropped into 0.1 M phosphoric acid (H<sub>3</sub>PO<sub>4</sub>) ethanol solution [35]. After stirring at 60 °C for 1 h, the obtained yellow precipitate was washed with ethanol several times, and the TE Ag<sub>3</sub>PO<sub>4</sub> powders were obtained. Subsequently, the Ag<sub>3</sub>PO<sub>4</sub> powders were added into a certain amount of g-C<sub>3</sub>N<sub>4</sub> dispersion. The mixture was sonicated for 30 min to completely disperse Ag<sub>3</sub>PO<sub>4</sub> crystals and then stirred until the ethanol was volatilized completely [36]. The obtained samples were referred to as xCA with x representing the weight ratios of g-C<sub>3</sub>N<sub>4</sub> and Ag<sub>3</sub>PO<sub>4</sub>, and x varied from 2% to 20%. For comparison, the "Blend" was fabricated by mechanically blending of g-C<sub>3</sub>N<sub>4</sub> and Ag<sub>3</sub>PO<sub>4</sub> ( $w_{g-C_3N_4}/w_{Ag_3PO_4}=10\%$ ). Meanwhile, irregular Ag<sub>3</sub>PO<sub>4</sub> crystals (IR Ag<sub>3</sub>PO<sub>4</sub>) were synthesized by direct precipitation method as follows: disodium hydrogen phosphate (Na<sub>2</sub>HPO<sub>4</sub>) solution was added drop by drop to the AgNO<sub>3</sub> solution under stirring. After stirring for 1 h, the above suspension experienced centrifugation, washing and drying.

### 2.3 Characterization

X-ray diffraction (XRD) patterns of the samples were identified using a Shimadzu XRD-6000 powder diffractometer (Cu K $\alpha$  radiation). The morphology observations were observed on a JSM-6390A scanning electron microscope (SEM) equipped with energy-dispersive X-ray (EDS) and a Tecnai G2F20S-TWIN transmission electron microscopy (TEM). Besides, the Fourier transform infrared spectra (FTIR) of the products were recorded using PerkinElmer Frontier. UV-Vis absorption spectra were recorded using a Shimadzu UV-3600 UV/VIS/NIR spectrophotometer with BaSO<sub>4</sub> as a reference. X-ray photoelectron spectroscopy (XPS) was obtained with a Kratos AXIS NOVA spectrometer. The surface areas of samples were measured using the Brunauer-Emmett-Teller (BET) method by N<sub>2</sub> adsorption Quantachrome NOVA 2000e, and photoluminescence (PL) measurements were carried out on a Hitachi F-7000 fluorescence spectrophotometer.

### 2.4 Photocatalytic degradation of MB

The as-obtained samples were evaluated by degradation of MB in aqueous solution under visible light irradiation. In a typical process, 40 mg photocatalysts were added into 50 mL MB solution (10 mg/L). Prior to irradiation, the suspensions were magnetically stirred in dark for 30 min to ensure the adsorption-desorption equilibrium of MB on the surface of the photocatalysts. 300 W xenon lamp (Microsolar 300) with a 400 nm cut off filter was used as visible light source, which was positioned on the top of the reaction cell. The above suspensions with air blown were photoirradiated under continuous stirring throughout the test at room temperature. At regular intervals, 2 mL suspensions were sampled and centrifuged, the upper clear liquid was evaluated according to the absorbance at recording the maximum absorption band (664 nm for MB) using a Shimadzu UV-3600 UV/Vis/NIR spectrophotometer.

### 2.5 Photocatalytic removal of NO

The photocatalytic experiments for NO removal were performed at ambient temperature in a continuous flow reactor [37] (Fig. S1, Supporting Information). For each experiment, 0.1 g catalyst powders were set in the center of the reactor by a dish with a diameter of 6.5 cm. The reactant gas mixture (the concentration of NO was 600 ppb) was fed into the reactor with a total flow rate of 400 mL/min, and the residence time of mixture gas in the reaction vessel was about 57 s. After the adsorption-desorption equilibrium was achieved, the 300 W xenon lamp (Microsolar 300) with a 400 nm cut off filter was turned on. The concentration of NO was continuously measured by an electrochemical NO analyzer (Shenzhen Jishunan Technology CO.LTD., JSA9-NO). The NO conversion ( $\eta$ ) was calculated as:  $\eta(\%) = (1 - C/C_0) \times 100\%$ , where  $C$  is the outlet concentration of NO after reaction for time  $t$ , and  $C_0$  represents the inlet concentration after achieving the adsorption-desorption equilibrium.

### 2.6 Active species trapping experiment

For the trapping of photogenerated active species during photocatalytic reactivity, hydroxyl radicals ( $\bullet$ OH), superoxide radical ( $O_2^{\bullet-}$ ) and holes ( $h^+$ ) were investigated using isopropanol (IPA, a quencher of  $\bullet$ OH), p-benzoquinone (BQ, a quencher of  $O_2^{\bullet-}$ ) and triethanolamine (TEOA, a quencher of  $h^+$ ) respectively [38]. The process of active species trapping experiment was similar to the MB

photodegradation experiment. Before adding the photocatalyst, scavengers were introduced into the MB solution respectively.

### 3 Results and discussion

#### 3.1 Characterization of the samples

X-ray diffraction (XRD) patterns of  $g\text{-C}_3\text{N}_4$ ,  $\text{Ag}_3\text{PO}_4$  and 10CA are shown in Fig. 1. For  $\text{C}_3\text{N}_4$  sample, the two peaks at  $13.1^\circ$  and  $27.4^\circ$  correspond to the (100) and (002) planes of the tetragonal phase  $g\text{-C}_3\text{N}_4$  (JCPDS 87-1526), respectively. All diffraction peaks of the  $\text{Ag}_3\text{PO}_4$  sample can be well indexed to the cubic-phase  $\text{Ag}_3\text{PO}_4$  (JCPDS 06-0505). The diffraction pattern of  $\text{Ag}_3\text{PO}_4$  shows peaks at  $21.1, 30.0, 33.6, 36.8, 42.7, 48.1, 52.9, 55.3, 57.5, 61.9, 66.1, 70.1, 72.1$  and  $74.1$ , which correspond to planes (110), (200), (210), (211), (220), (310), (222), (320), (321), (400), (330), (420), (421) and (332), respectively. There are no peaks of impurities, and the strong and sharp peaks indicate the high crystallinity of the  $\text{Ag}_3\text{PO}_4$  sample. The XRD pattern of the 10CA is similar to that of the bare  $\text{Ag}_3\text{PO}_4$ , and the characteristic peaks of  $g\text{-C}_3\text{N}_4$  are not observed due to the exfoliation of  $g\text{-C}_3\text{N}_4$  [25].

The surface morphologies of  $g\text{-C}_3\text{N}_4$ ,  $\text{Ag}_3\text{PO}_4$  and  $g\text{-C}_3\text{N}_4/\text{Ag}_3\text{PO}_4$  {111} are shown in Fig. 2. As shown in Fig. 2a, the synthesized TE  $\text{Ag}_3\text{PO}_4$  samples are tetrahedral particles with the particle size of  $0.4 \sim 2.1 \mu\text{m}$  and average size of  $0.74 \mu\text{m}$ , and the tetrahedron is enclosed completely by four perfect equilateral triangles, which consists of {111} facets. IR  $\text{Ag}_3\text{PO}_4$  are near-spherical particles with the particle size of  $0.3 \sim 1 \mu\text{m}$  (Fig. 2b). Fig. 2c and Fig. 2e show the SEM and TEM images of pure  $g\text{-C}_3\text{N}_4$ , and the gauze-like and sheet-like morphology can be clearly observed, indicating that  $g\text{-C}_3\text{N}_4$  nanosheets with few-layer structure can be prepared by a simple chemical exfoliation process. In the  $g\text{-C}_3\text{N}_4/\text{Ag}_3\text{PO}_4$  {111} hybrid (Fig. 2d and Fig. 2f),  $g\text{-C}_3\text{N}_4$  is overlaid on the surface of  $\text{Ag}_3\text{PO}_4$  particles or scattered around  $\text{Ag}_3\text{PO}_4$  particles. During ultrasonication and ethanol evaporation process, the  $g\text{-C}_3\text{N}_4$  assembled on the surface of  $\text{Ag}_3\text{PO}_4$  or gathered around  $\text{Ag}_3\text{PO}_4$  to achieve a minimum surface energy [39,40]. Comparing with the pure  $\text{Ag}_3\text{PO}_4$ , the  $g\text{-C}_3\text{N}_4$  not only prevents the agglomeration of  $\text{Ag}_3\text{PO}_4$  particles, but also forms heterojunction with  $\text{Ag}_3\text{PO}_4$  in the composite. The morphology studies revealed that  $g\text{-C}_3\text{N}_4$  could serve as a support to bound  $\text{Ag}_3\text{PO}_4$  particles in the hybrid system, which leads to the formation of interfacial contact between  $g\text{-C}_3\text{N}_4$  and  $\text{Ag}_3\text{PO}_4$  and to favorable photogenerated charge transfer at the

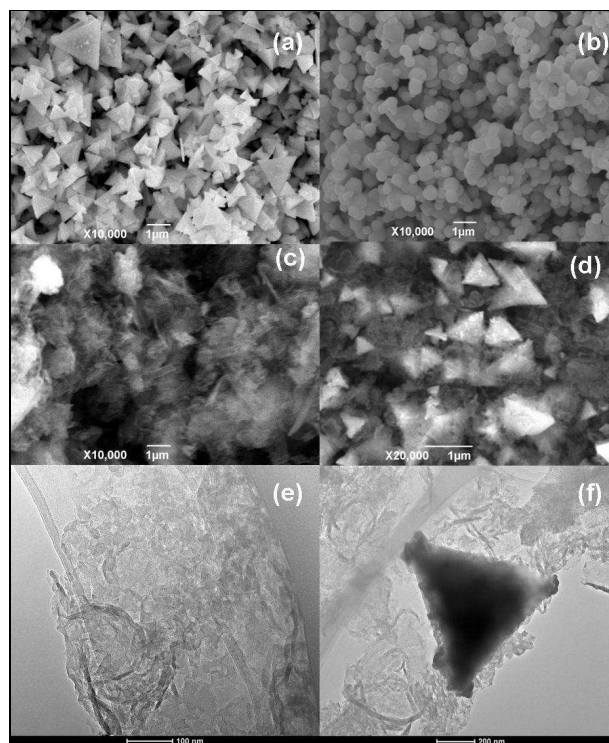


Fig. 2 SEM and TEM images of samples: (a) and (b) TE  $\text{Ag}_3\text{PO}_4$  and IR  $\text{Ag}_3\text{PO}_4$ , (c) and (d) SEM of  $g\text{-C}_3\text{N}_4$  and 10CA, (e) and (f) TEM of  $g\text{-C}_3\text{N}_4$  and 10CA.

interface when using as hybrid photocatalyst. The energy-dispersive X-ray spectrometry (EDS) analysis of 10CA hybrid is shown in Fig. S3, and C, N, O, P and Ag as major elements are detected from sample, further suggesting the existence of  $\text{C}_3\text{N}_4$  and  $\text{Ag}_3\text{PO}_4$ .

The FT-IR spectra of  $g\text{-C}_3\text{N}_4$ ,  $\text{Ag}_3\text{PO}_4$  and  $g\text{-C}_3\text{N}_4/\text{Ag}_3\text{PO}_4$  hybrids are shown in Fig. 3. For the pristine  $g\text{-C}_3\text{N}_4$ , it reveals a typical molecular structure of graphitic carbon nitride. The peaks at  $1634, 1574, 1460, 1405, 1317$  and  $1238 \text{ cm}^{-1}$  are attributed to the typical stretching modes of C-N heterocycles, and the peak at  $807 \text{ cm}^{-1}$  is the characteristic breathing mode of triazine units [41]. The broad band at  $3000\text{-}3400 \text{ cm}^{-1}$  is due to uncondensed terminal amino groups ( $-\text{NH}_2$  or  $=\text{NH}$  groups) at the defect sites of the aromatic ring [42]. For pure  $\text{Ag}_3\text{PO}_4$ , the observed strong peaks at  $548$  and  $951 \text{ cm}^{-1}$  may be attributed to the characteristic peaks of  $\text{PO}_4^{3-}$ . In addition, all characteristic peaks corresponding to  $g\text{-C}_3\text{N}_4$  and

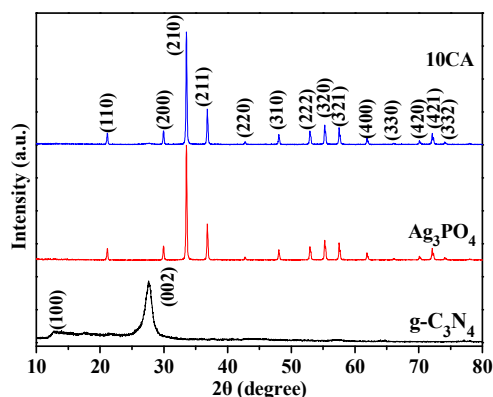


Fig. 1. XRD patterns of  $g\text{-C}_3\text{N}_4$ ,  $\text{Ag}_3\text{PO}_4$  and 10CA.

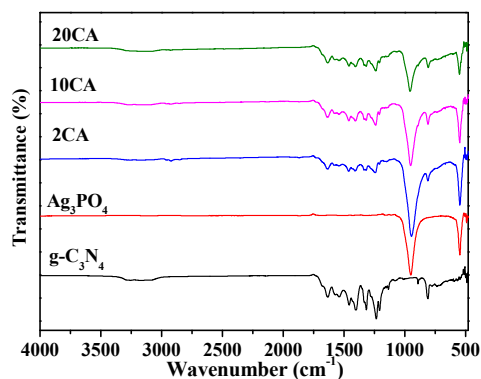


Fig. 3 FT-IR spectra of  $g\text{-C}_3\text{N}_4$ ,  $\text{Ag}_3\text{PO}_4$  and  $g\text{-C}_3\text{N}_4/\text{Ag}_3\text{PO}_4$  {111} hybrid.

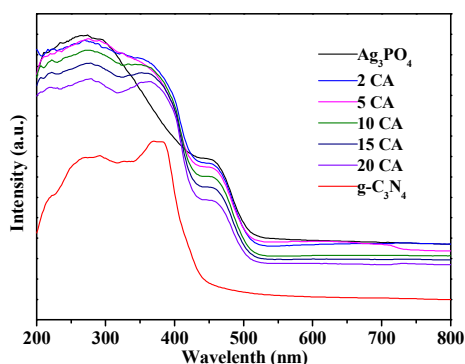


Fig. 4 UV-Vis absorption spectra of samples.

$\text{Ag}_3\text{PO}_4$  appear in  $\text{g-C}_3\text{N}_4/\text{Ag}_3\text{PO}_4$  hybrids, and the relative intensity of the peaks of  $\text{g-C}_3\text{N}_4$  increases with the increase of  $\text{g-C}_3\text{N}_4$  contents in composites.

The UV-Vis absorption spectra of the samples were investigated and shown in Fig. 4. Pure  $\text{g-C}_3\text{N}_4$  can absorb visible light with wavelengths shorter than 440 nm, whereas pure  $\text{Ag}_3\text{PO}_4$  has a broader absorption in the visible region with an absorption edge at about 530 nm. The  $\text{g-C}_3\text{N}_4/\text{Ag}_3\text{PO}_4$  hybrids exhibit the two absorption edges at both 440 and 530 nm, suggesting that these samples contain both  $\text{g-C}_3\text{N}_4$  and  $\text{Ag}_3\text{PO}_4$  semiconductors.

According to the plot of  $(F(R)h\nu)^{1/2}$  vs  $h\nu$ , the band gaps ( $E_g$ ) of  $\text{Ag}_3\text{PO}_4$  and  $\text{g-C}_3\text{N}_4$  were estimated to be 2.51 and 3.08 eV, respectively (Fig. S3, Supporting Information). The band structure of  $\text{g-C}_3\text{N}_4$  and  $\text{Ag}_3\text{PO}_4$  can be estimated according to the empirical equations [43] as shown below:

$$E_{VB} = \chi - E_e + 0.5E_g$$

$$E_{CB} = E_{VB} - E_g$$

where  $E_{VB}$  and  $E_{CB}$  are the valence and conduction band edge potentials, respectively;  $\chi$  is the absolute electronegativity of the semiconductor, expressed as the geometric mean of the absolute

Table 1 Calculation of the CB and VB potentials of  $\text{Ag}_3\text{PO}_4$  and  $\text{g-C}_3\text{N}_4$ .

	$\chi$	$E_g$ (eV)	$E_{CB}$ (eV)	$E_{VB}$ (eV)
$\text{Ag}_3\text{PO}_4$	5.96	2.51	0.21	2.72
$\text{g-C}_3\text{N}_4$	4.72	3.08	-1.32	1.76

electronegativity of the constituent atoms, and defined as the arithmetic mean of the atomic electro affinity and the first ionization energy;  $E_e$  is the energy of free electrons on the hydrogen scale (about 4.5 eV vs NHE);  $E_g$  is the band gap energy of the semiconductor. Thus, the calculated values of the CB and VB potentials of  $\text{Ag}_3\text{PO}_4$  and  $\text{g-C}_3\text{N}_4$  are listed in Table 1.

The elemental composition and chemical status of 10CA were further characterized by X-ray photoelectron spectroscopy (XPS), as shown in Fig. 5. It is found that the two C 1s peaks are located at 284.6 and 288.1 eV, respectively (Fig. 5a). The former is ascribed to the contaminated carbons, whereas the latter one is assigned to  $\text{sp}^2$ -bonded carbon ( $\text{N-C}=\text{N}$ ) [38]. The N 1s peaks can be deconvoluted into three fitted peaks at binding energies of 398.1 (N1), 399.6 (N2) and 403.9 eV (N3) (Fig. 5b), respectively. The dominant N1 is commonly attributed to  $\text{sp}^2$  N atoms involved in triazine rings, while the N2 is assigned to bridging N atoms in  $\text{N}(\text{C})_3$  or N bonded with H atoms. The very weak N3 can be assigned to the charging effects or positive charge localization in heterocycles and the cyano-group [44]. As shown in Fig. 5c, the peaks of Ag 3d<sub>5/2</sub> and Ag 3d<sub>3/2</sub> are located at 368 and 374 eV, respectively. These two bands could be further deconvoluted into two peaks. The strong peaks at 367.8 and 373.8 eV are assigned to  $\text{Ag}^+$  of  $\text{Ag}_3\text{PO}_4$ , while the weak peaks at 369.2 and 375.3 eV belongs to the metallic  $\text{Ag}^0$  species [45], which originates in the formed metallic Ag during the hybrid preparation. Because  $\text{g-C}_3\text{N}_4$  has the electron-rich structure, and {111} facets of  $\text{Ag}_3\text{PO}_4$  only contain  $\text{Ag}^+$  cations proved by the surface atomic configurations studies [46],  $\text{g-C}_3\text{N}_4$

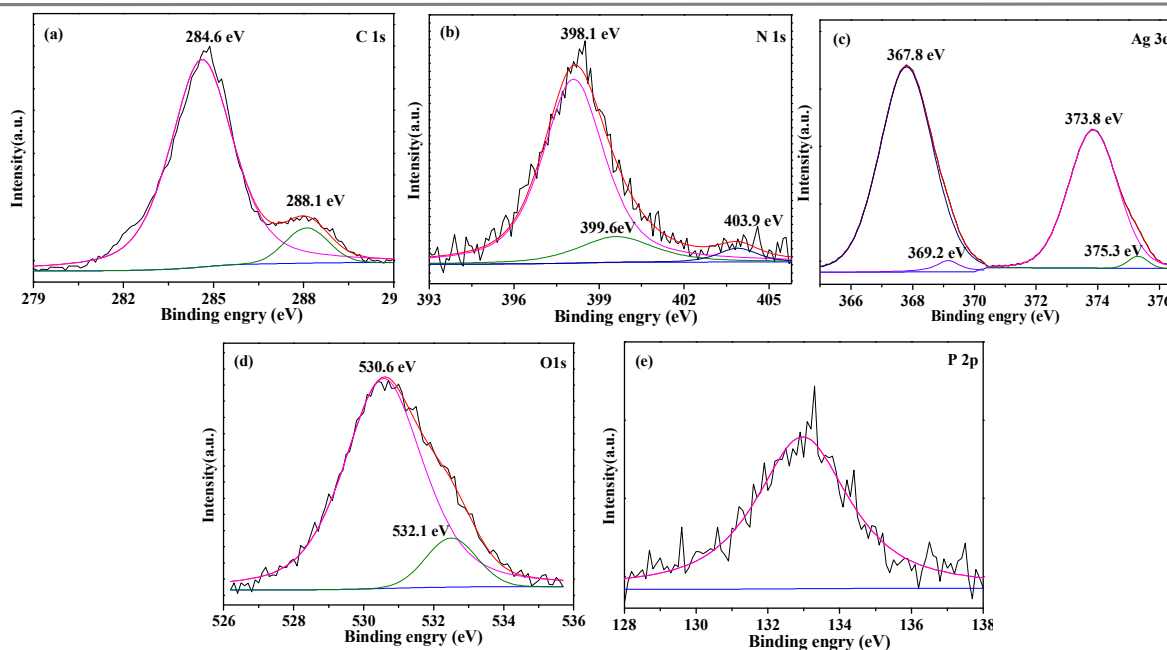


Fig. 5 XPS spectra of 10CA: (a) C 1s, (b) N 1s, (c) Ag 3d, (d) O 1s, (e) P 2p.

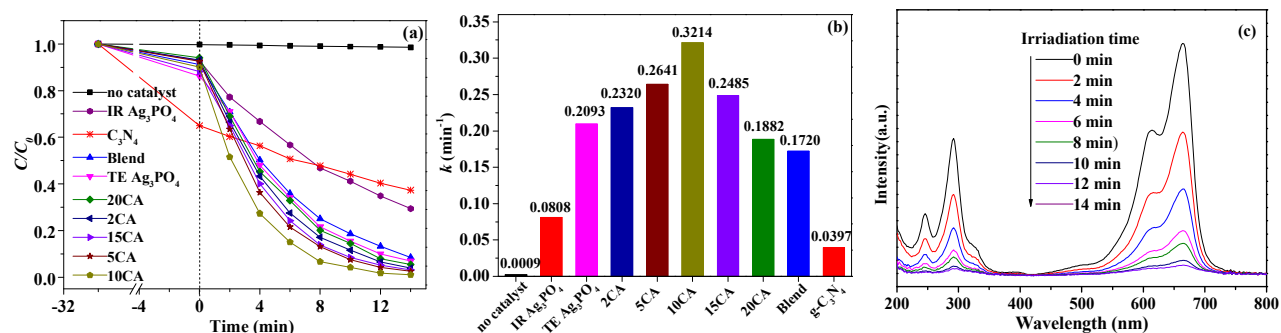


Fig. 6 (a) Photocatalytic degradation curves of MB over samples under the visible-light irradiation (> 400 nm); (b) the kinetic constants of photocatalysts; (c) UV-Visible spectra of MB at different visible irradiation times in the presence of 10CA.

can easily provide electrons to Ag<sup>+</sup> on the surface of Ag<sub>3</sub>PO<sub>4</sub> to form Ag<sup>0</sup> particles which contact with both Ag<sub>3</sub>PO<sub>4</sub> and g-C<sub>3</sub>N<sub>4</sub> in the hybrid catalyst. For the O 1s (Fig. 5d), the peak at 530.6 eV is assigned to the crystal lattice oxygen, while the peak at 532.1 eV is related to adsorbed oxygen [45], which favours the degradation of organic pollutants in water and gaseous pollutants in the gas phase. The spectrum of P 2p is shown in Fig. 5e, and a broad peak in the range of 130 to 136 eV appears to be attributable to the P element in PO<sub>4</sub><sup>3-</sup> [47].

### 3.2 Photocatalytic degradation of MB

Photocatalytic tests of samples were evaluated by degradation of MB under visible light irradiation ( $\lambda > 400$  nm), and the results are shown in Fig. 6. Fig. 6a shows the remaining MB in solution after adsorption equilibrium and the MB degradation ( $C/C_0$ ) with the irradiation time over the catalysts. After adsorption equilibrium, 65%, 94% and 90% of MB remains in the solution with the g-C<sub>3</sub>N<sub>4</sub>, Ag<sub>3</sub>PO<sub>4</sub> and 10CA photocatalysts, respectively, and the adsorptive ability of g-C<sub>3</sub>N<sub>4</sub>/Ag<sub>3</sub>PO<sub>4</sub> hybrids increases with the increasing contents of g-C<sub>3</sub>N<sub>4</sub> in composites. It is obvious that g-C<sub>3</sub>N<sub>4</sub> has superior adsorptive ability because aromatic molecules such as MB could be adsorbed on the g-C<sub>3</sub>N<sub>4</sub> surface with offset face to face orientation via  $\pi$ - $\pi$  conjugation until an adsorption-desorption equilibrium is reached. By modification with g-C<sub>3</sub>N<sub>4</sub>, the adsorptivity of Ag<sub>3</sub>PO<sub>4</sub> to MB is enhanced, which is beneficial to the photodecomposition of MB. MB self-photolysis without catalyst under visible light irradiation is not observable, which indicates that MB self-photolysis is negligible in the process of photocatalysis. It can be found that the photocatalytic activity of 10CA is the highest among all samples under visible light irradiation: about 99 % of MB is photocatalytically degraded after 14 minutes irradiation. A pseudo-first-order kinetic model was employed to fit the degradation data by using the equation [12]:  $-\ln(C/C_0) = kt$ , where  $k$  is the apparent reaction rate constant (min<sup>-1</sup>), and  $C$  and  $C_0$  are the adsorption equilibrium concentration and MB concentration at reaction time  $t$ . The results are illustrated in Fig. 6(b). It can be clearly seen that the TE Ag<sub>3</sub>PO<sub>4</sub> (0.2093 min<sup>-1</sup>) shows better photocatalytic activities than that of IR Ag<sub>3</sub>PO<sub>4</sub> (0.0808 min<sup>-1</sup>), and the  $k$  of TE Ag<sub>3</sub>PO<sub>4</sub> is about 2.59 times higher than that of IR Ag<sub>3</sub>PO<sub>4</sub> due to the higher surface energy and more active sites of {111} facets. Meanwhile, except for 20CA, the photocatalytic activities of g-C<sub>3</sub>N<sub>4</sub>/Ag<sub>3</sub>PO<sub>4</sub> hybrids are higher than that of bare Ag<sub>3</sub>PO<sub>4</sub>, greatly depending on the g-C<sub>3</sub>N<sub>4</sub> content. The

photodegradation rates first increase and then decrease with rising g-C<sub>3</sub>N<sub>4</sub> content, and 10CA displays the highest degradation rate. The  $k$  of 10CA is 0.3214 min<sup>-1</sup>, which is 1.54 and 8.10 times as high as that of pure Ag<sub>3</sub>PO<sub>4</sub> (0.2093 min<sup>-1</sup>) and pure g-C<sub>3</sub>N<sub>4</sub> (0.0397 min<sup>-1</sup>). In addition, the "Blend" ( $w_{g-C_3N_4}/w_{Ag_3PO_4} = 10\%$ ) is labeled as for reference to explain the difference in physical mixture and hybrid from solvent evaporation process. The "Blend" exhibits similar adsorptivity to the hybrid, while it shows related lower photocatalytic performance than 10CA, even lower than pure Ag<sub>3</sub>PO<sub>4</sub>. These results clearly demonstrate that the remarkable enhancement of photoactivity is only achieved when hybridized with g-C<sub>3</sub>N<sub>4</sub> by the solvent evaporation process and the interfacial interaction between these two components in the hybrid makes the photocatalytic reaction more efficient than that in physical mixture. Moreover, Fig S6a shows photocatalytic degradation of MB over

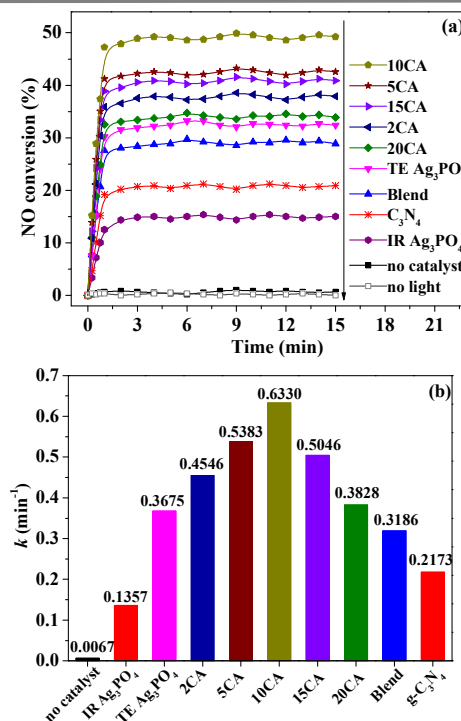


Fig. 7 (a) Plots of the removal ratio of NO vs irradiation time on different photocatalysts under visible light (> 400 nm); (b) reaction rate constant (min<sup>-1</sup>) in the presence of the as-prepared photocatalysts under visible light (> 400 nm).

$g\text{-C}_3\text{N}_4/\text{Ag}_3\text{PO}_4(\text{IR})$ ,  $\text{BiVO}_4$  and P25 under the visible light irradiation ( $> 400$  nm).  $g\text{-C}_3\text{N}_4/\text{Ag}_3\text{PO}_4\{111\}$  showed obvious higher photocatalytic performance than that of  $g\text{-C}_3\text{N}_4/\text{Ag}_3\text{PO}_4(\text{IR})$  and dramatically higher than that of  $\text{BiVO}_4$  and P25, indicating the photocatalytic performance in the single material (TE  $\text{Ag}_3\text{PO}_4$ ) is still maintained in the heterojunction and the high efficiency of  $\text{C}_3\text{N}_4/\text{Ag}_3\text{PO}_4\{111\}$  for photocatalytic degradation of MB.

### 3.3 Photocatalytic removal of NO

NO in low concentration ppb levels are representative of indoor and outdoor air pollutants. The as-prepared samples were employed in the photocatalytic removal of NO from air to investigate their potential capability for gas-phase pollutant degradation. Fig. 7 shows the photodegrading NO ability of samples. It is found that the photolysis of NO without light or without photocatalyst under visible light irradiation is negligible, indicating removal NO is a photocatalytic process. It is obvious from Fig. 7a that the rapid increase in NO conversion with irradiation time is observed over all the photocatalysts, and then approach a steady state. For pure  $g\text{-C}_3\text{N}_4$ , IR  $\text{Ag}_3\text{PO}_4$  and TE  $\text{Ag}_3\text{PO}_4$  samples, 20.9%, 15.0% and 32.4% removal of NO is obtained at continuous system. In the case of  $\text{Ag}_3\text{PO}_4$  hybridized with  $g\text{-C}_3\text{N}_4$ , the removal ratios of NO increase. The  $g\text{-C}_3\text{N}_4/\text{Ag}_3\text{PO}_4\{111\}$  removal ability of NO improves with the increase of  $g\text{-C}_3\text{N}_4$  content, and then decrease with the further added. The optimal rate of  $g\text{-C}_3\text{N}_4$  and  $\text{Ag}_3\text{PO}_4$  is 10%, whose removal ratio of NO is 49.3%. The removal ratio of NO of "Blend" is 28.9%, which is much lower than that of the 10CA heterojunction, implying that the heterojunction formed between  $\text{Ag}_3\text{PO}_4$  and  $g\text{-C}_3\text{N}_4$  plays a major role in improving the photocatalytic activity. In order to produce a further comparison

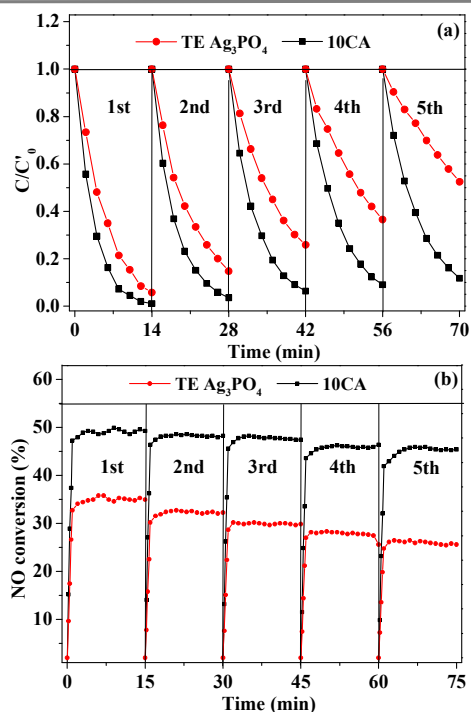


Fig. 8. Cycling runs for the photocatalytic activity over pure  $\text{Ag}_3\text{PO}_4$  and 10CA under visible light irradiation: (a) photocatalytic degradation of MB; photocatalytic removal of NO.

among the tested samples, first order rate constants were calculated from the experimental data relative to the first 1 min of irradiation [48,49]. The data are displayed in Fig. 7b. It can be clearly seen that the  $k$  of TE  $\text{Ag}_3\text{PO}_4$  ( $0.3675 \text{ min}^{-1}$ ) is about 2.71 times higher than that of IR  $\text{Ag}_3\text{PO}_4$  ( $0.1357 \text{ min}^{-1}$ ), the  $k$  of 10CA ( $0.633 \text{ min}^{-1}$ ) is nearly 1.72 and 2.91 times higher than that of pure TE  $\text{Ag}_3\text{PO}_4$  and  $g\text{-C}_3\text{N}_4$  ( $0.2173 \text{ min}^{-1}$ ), respectively. Furthermore, the performance of photocatalytic removal of NO over  $g\text{-C}_3\text{N}_4/\text{Ag}_3\text{PO}_4(\text{IR})$ ,  $\text{BiVO}_4$  and P25 under the visible light irradiation ( $> 400$  nm) are shown in Fig. 6Sb. Fig. 6Sb shows  $g\text{-C}_3\text{N}_4/\text{Ag}_3\text{PO}_4\{111\}$  has obvious higher photocatalytic performance than that of  $g\text{-C}_3\text{N}_4/\text{Ag}_3\text{PO}_4(\text{IR})$ ,  $\text{BiVO}_4$  and P25.

The reusability and stability of the as-synthesized photocatalyst was studied by the circulating runs, and they were performed five times on 10%  $g\text{-C}_3\text{N}_4/\text{Ag}_3\text{PO}_4\{111\}$  and pure  $\text{Ag}_3\text{PO}_4$  samples. The corresponding results are shown in Fig. 8. As exhibited in Fig. 8a, the photocatalytic performance of pure  $\text{Ag}_3\text{PO}_4$  shows a significant reduction during the repeated photocatalytic reactions, but the photocatalytic activity of the 10CA shows just a little loss after five cycling runs of photodegradation of MB. Fig. 7(b) shows after 5 successive NO degradation, the photocatalytic activities of the 10CA is evidently more stable than that of pure  $\text{Ag}_3\text{PO}_4$ . There are two possible reasons to explain the enhanced stabilities of  $g\text{-C}_3\text{N}_4/\text{Ag}_3\text{PO}_4$  hybrid photocatalysts compared with pure  $\text{Ag}_3\text{PO}_4$  crystals. First,  $\text{C}_3\text{N}_4$  coated on the surface of  $\text{Ag}_3\text{PO}_4$  or scattered around  $\text{Ag}_3\text{PO}_4$  can inhibit the dissolution of  $\text{Ag}_3\text{PO}_4$  in aqueous solution, which will enhance its structural stability. Second, the photocatalytic performance deteriorates quickly is due to the photo-corrosion of pure  $\text{Ag}_3\text{PO}_4$  particles by the rich excited electrons on the surface of  $\text{Ag}_3\text{PO}_4$ . However, the rich excited electrons on the surface of  $\text{Ag}_3\text{PO}_4$  in the  $g\text{-C}_3\text{N}_4/\text{Ag}_3\text{PO}_4$  hybrids are transferred by the special structure of the  $g\text{-C}_3\text{N}_4/\text{Ag}_3\text{PO}_4$  hybrids resulting in preventing  $\text{Ag}_3\text{PO}_4$  from photo-corrosion.

### 3.4 Photocatalytic mechanism

It is well known that the high surface area and high separation efficiency of photogenerated electrons and holes are beneficial for the photocatalytic activity. Fig. S5 shows the nitrogen adsorption-desorption isotherms of pure  $\text{Ag}_3\text{PO}_4$  and 10CA. The specific surface area of pure  $\text{Ag}_3\text{PO}_4$  is  $4.1 \text{ m}^2/\text{g}$ . After coupling  $\text{Ag}_3\text{PO}_4$  particles with  $g\text{-C}_3\text{N}_4$ , the specific surface area increases to  $11.2 \text{ m}^2/\text{g}$ . Meanwhile, PL spectrum analysis was carried out to investigate the separation efficiency of photogenerated electrons

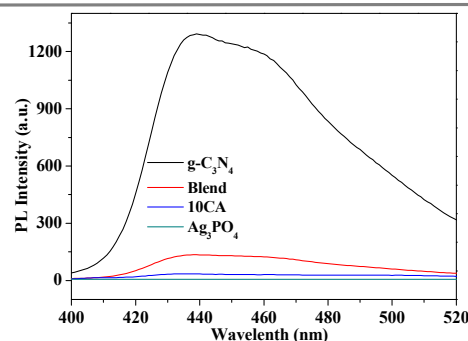


Fig. 9. Photoluminescence spectra of  $g\text{-C}_3\text{N}_4$ , Blend, 10CA and  $\text{Ag}_3\text{PO}_4$  samples excited by 270 nm.

and holes in photocatalysts. Fig. 9 shows the PL spectra of the pure  $g\text{-C}_3\text{N}_4$ , pure  $\text{Ag}_3\text{PO}_4$ , Blend and 10CA. Pure  $g\text{-C}_3\text{N}_4$  exhibits a strong emission with an emission peak at about 441 nm, which was similar to the literatures [41]. Compared with  $g\text{-C}_3\text{N}_4$ , the PL intensities of pure  $\text{Ag}_3\text{PO}_4$  and 10CA are much weaker, reflecting their slow recombination rates of photogenerated electron-hole pairs. Although the PL intensity of 10CA is slightly higher than that of pure  $\text{Ag}_3\text{PO}_4$ , it is much weaker than that of the "Blend", which suggests heterojunction between  $\text{Ag}_3\text{PO}_4$ , Ag and  $g\text{-C}_3\text{N}_4$  is effectively formed during the solvent evaporation process and it benefits to the separation of electron-hole pairs. The PL results are in accordance with the photocatalytic activity of the catalysts.

In order to deduce the migration path of the photogenerated electrons and holes in the composites, the active species trapping experiments were conducted. When bare  $\text{Ag}_3\text{PO}_4$  is used as photocatalyst, the photodegradation of MB is significantly suppressed by the introduction of TEOA (a quencher of  $h^+$ ), indicating that holes are the main reactive oxidative species involved in the photocatalysis, which is consistent with reports that the oxidation mechanism of  $\text{Ag}_3\text{PO}_4$  proceeds through direct  $h^+$  attack to target organic compounds. In contrast, the adding of BQ (a quencher of  $\text{O}_2^{\bullet-}$ ) or IPA (a quencher of  $\bullet\text{OH}$ ) in the solution has no obvious effect on the photocatalytic activity of  $\text{Ag}_3\text{PO}_4$  (Fig. 10), implying that  $\text{O}_2^{\bullet-}$  and  $\bullet\text{OH}$  radicals have no contribution to the degradation process. The photocatalytic behavior of  $g\text{-C}_3\text{N}_4/\text{Ag}_3\text{PO}_4$  is similar to that of bare  $\text{Ag}_3\text{PO}_4$  when TEOA or IPA is introduced into the photoreaction. However, the adding of BQ results in an unneglectable deactivation, indicating that besides holes,  $\text{O}_2^{\bullet-}$  radicals are also involved in the photocatalytic process. For pure  $g\text{-C}_3\text{N}_4$ , it can be found that the photodegradation rates decrease in the order: BQ ( $\text{O}_2^{\bullet-}$ ) < TEOA ( $h^+$ ) < IPA ( $\bullet\text{OH}$ ). It can

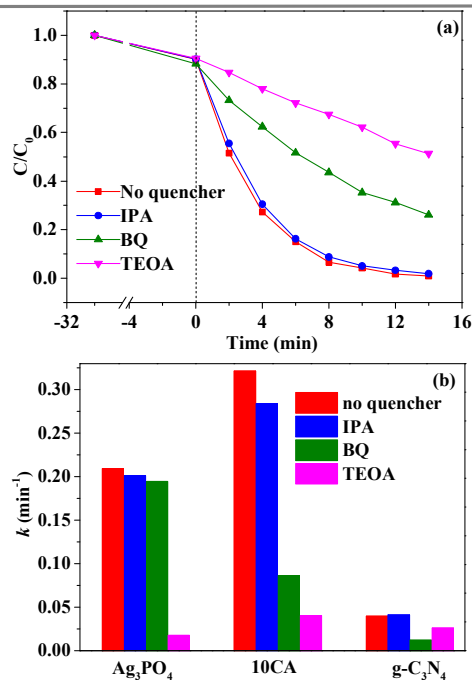


Fig. 10 (a) Photocatalytic degradation curves of MB over 10CA with different quenchers; (b) the kinetic constants of  $\text{Ag}_3\text{PO}_4$ , 10CA and  $g\text{-C}_3\text{N}_4$  photocatalysts with different quenchers.

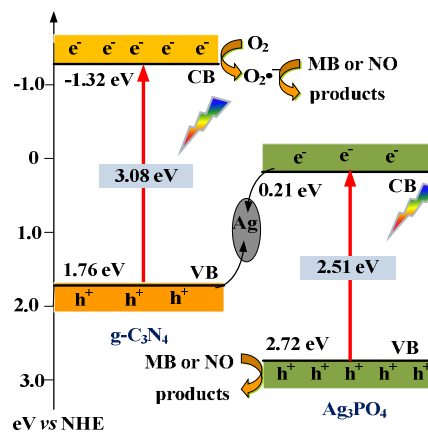


Fig. 11 Photocatalytic mechanism scheme of the  $g\text{-C}_3\text{N}_4/\text{Ag}_3\text{PO}_4$  {111} hybrid.

be concluded that photogenerated holes ( $h^+$ ) are the most main active species and  $\text{O}_2^{\bullet-}$  radicals are the second main active species in the photocatalytic process. Considering the CB and VB potentials of  $\text{Ag}_3\text{PO}_4$  and  $g\text{-C}_3\text{N}_4$ , the photoexcited electrons on the CB of  $g\text{-C}_3\text{N}_4$  in  $g\text{-C}_3\text{N}_4/\text{Ag}_3\text{PO}_4$  composites could flow directly to the CB of  $\text{Ag}_3\text{PO}_4$  and accumulate on the CB of  $\text{Ag}_3\text{PO}_4$ , but it results in the dominant reactive species of  $h^+$ , which is inconsistent with the experimental result. Therefore, photoexcited electrons on the CB of  $g\text{-C}_3\text{N}_4$  do not flow directly into CB of  $\text{Ag}_3\text{PO}_4$  but enrich on the CB of  $g\text{-C}_3\text{N}_4$  through other mechanism (thereby retaining sufficient capacity to reduce  $\text{O}_2$  species to  $\text{O}_2^{\bullet-}$ ).

Based on the above results, a possible mechanism for photocatalytic degradation MB and removal NO on  $g\text{-C}_3\text{N}_4/\text{Ag}_3\text{PO}_4$  hybrid photocatalyst was proposed in Fig. 11. It can be ascribed to the efficient separation of photogenerated electrons and holes through the Z-scheme system composed of  $\text{Ag}_3\text{PO}_4$ , Ag and  $g\text{-C}_3\text{N}_4$ . A similar Z-scheme mechanism for  $\text{Ag}@\text{AgBr}/g\text{-C}_3\text{N}_4$  composite photocatalysts has been reported by other researchers [50]. Under visible light irradiation, both  $\text{Ag}_3\text{PO}_4$  and  $g\text{-C}_3\text{N}_4$  are excited to generate photogenerated electrons ( $e^-$ ) and holes ( $h^+$ ), respectively. Because metallic  $\text{Ag}^0$  formed on the surface of  $\text{Ag}_3\text{PO}_4$  can act as a charge transmission bridge, the  $e^-$  of  $\text{Ag}_3\text{PO}_4$  can easily flow into metal Ag and then continually transfer to the VB of  $g\text{-C}_3\text{N}_4$ , making charge separation more efficient. Therefore, the Z-scheme mechanism is established, which keeps  $e^-$  on the CB of  $g\text{-C}_3\text{N}_4$  high reduction capability and  $h^+$  on VB of  $\text{Ag}_3\text{PO}_4$  strong oxidation capability. Because  $E_{\text{CB}}(g\text{-C}_3\text{N}_4, -1.32 \text{ eV})$  is more negative than the standard reduction potential of  $\text{O}_2/\text{O}_2^{\bullet-}$  ( $E^0(\text{O}_2/\text{O}_2^{\bullet-}) = +0.13 \text{ eV}$ ), the  $e^-$  of  $g\text{-C}_3\text{N}_4$  can further react with dissolved  $\text{O}_2$  to form  $\text{O}_2^{\bullet-}$  radicals, which can further oxidize pollutants. Considering that the CB potential of  $\text{Ag}_3\text{PO}_4$  (0.21 eV) is higher than the potential of  $\text{O}_2/\text{O}_2^{\bullet-}$ , the electrons in the CB of pure  $\text{Ag}_3\text{PO}_4$  can not reduce dissolved  $\text{O}_2$  to  $\text{O}_2^{\bullet-}$  through one-electron reduction. Clearly, the electron can enrich on the CB of  $g\text{-C}_3\text{N}_4$  only when the electron and holes in  $g\text{-C}_3\text{N}_4/\text{Ag}_3\text{PO}_4$  migrate by the Z-scheme mechanism. Meanwhile, the potential of the  $E_{\text{VB}}$  of  $\text{Ag}_3\text{PO}_4$  (2.72 eV) is near  $E^0(\bullet\text{OH}, \text{H}^+/\text{H}_2\text{O}) = 2.72 \text{ eV}$ , so the holes stayed on the VB of  $\text{Ag}_3\text{PO}_4$  can not react with  $\text{H}_2\text{O}$  to form  $\bullet\text{OH}$  radicals, which would photocatalytic oxidize pollutants directly [32]. By this manner, the photoexcited electron-holes in

the composite are separated efficiently, thereby leading to the excellent photocatalytic activity.

## 4 Conclusions

In summary, the reactive {111} facets of tetrahedral  $\text{Ag}_3\text{PO}_4$  microcrystals were hybridized with  $\text{g-C}_3\text{N}_4$  in the facile solvent evaporation process. The photocatalytic experiments indicated that the as-prepared  $\text{g-C}_3\text{N}_4/\text{Ag}_3\text{PO}_4$  exhibited significantly enhanced photocatalytic activity than that of pure  $\text{g-C}_3\text{N}_4$  and  $\text{Ag}_3\text{PO}_4$  samples toward photocatalytic degradation of methyl blue (MB) in aqueous solution and removal of NO at the indoor air level under visible light irradiation ( $> 400$  nm), and 10CA had the highest activity. The photocatalytic activity enhancement of  $\text{g-C}_3\text{N}_4/\text{Ag}_3\text{PO}_4$  hybrid photocatalysts could be ascribed to the combined effect of reactive {111} facets and the efficient separation of electron-hole pairs through a Z-scheme system composed of  $\text{Ag}_3\text{PO}_4$ , Ag and  $\text{g-C}_3\text{N}_4$ , in which Ag particles act as the charge separation center. Furthermore,  $\text{h}^+$  and  $\text{O}_2^-$  played the major role in photocatalysis process. This work suggests that the synthesized  $\text{g-C}_3\text{N}_4/\text{Ag}_3\text{PO}_4$  {111} hybrid is a promising visible light driven photocatalytic material for the photocatalytic removal of NO in the gas phase as well as the environmental purification of organic pollutants in aqueous solution.

## Acknowledgments

This work was supported by the National Natural Science Foundation of China (Nos. 21476183, 21176199, 21306150 and 51372201), the Specialized Research Fund for the Doctoral Program of Higher Education of China (No. 20136101110009), the Shaanxi Provincial Research Foundation for Basic Research of China (Nos. 2015JM5159), and the Research and Development Project of Shaanxi Institute of Technology (Gfy15-20).

## References

- 1 C. C. Chen, W. Ma and J. C. Zhao, *Chem. Soc. Rev.*, 2010, **39**, 4206-4219.
- 2 D. Q. Zhang, G. S. Li and J. C. Yu, *J. Mater. Chem.*, 2010, **20**, 4529-4536.
- 3 Z. G. Yi, J. H. Ye, N. Kikugawa, T. Kako, S. X. Ouyang, H. Stuart-Williams, H. Yang, J. C. Cao, W. J. Luo, Z. S. Li, Y. Liu and R. L. Withers, *Nat. Mater.*, 2010, **9**, 559-564.
- 4 Y. P. Bi, S. X. Ouyang, N. Umezawa, J. Y. Cao and J. H. Ye, *J. Am. Chem. Soc.*, 2011, **133**, 6490-6492.
- 5 H. Wang, L. He, L. H. Wang, P. F. Hu, L. Guo, X. D. Han and J. H. Li, *CrystEngComm*, 2013, **14**, 8342-8344.
- 6 Z. B. Jiao, Y. Zhang, H. C. Yu, G. X. Lu, J. H. Ye and Y. P. Bi, *Chem. Commun.*, 2013, **49**, 636-638.
- 7 Y. K. Jo, I. Y. Kim, J. M. Lee, S. Nahm, J. W. Choi and S. J. Hwang, *Mater. Lett.*, 2014, **114**, 152-155.
- 8 S. N. Zhang, S. J. Zhang and L. M. Song, *Appl. Catal. B-Environ.*, 2014, **152**, 129-139.
- 9 C. N. Tang, E. Z. Liu, J. Fan, X. Y. Hu, L. M. Kang and J. Wan, *Ceram. Int.*, 2014, **40**, 15447-15453.
- 10 T. J. Yan, W. F. Guan, W. J. Li and J. M. You, *RSC Adv.*, 2014, **4**, 37095-37099.
- 11 C. Dong, K. L. Wu, M. R. Li, L. Liu and X. W. Wei, *Catal. Comm.*, 2014, **46**, 32-35.
- 12 Z. M. Yang, G. F. Huang, W. Q. Huang, J. M. Wei, X. G. Yan, Y. Y. Liu, C. Jiao, Z. Wan and A. L. Pan, *J. Mater. Chem. A*, 2014, **2**, 1750-1756.
- 13 Y. H. Yan, H. Y. Guan, S. Liu and R. Y. Jiang, *Ceram. Int.*, 2014, **40**, 9095-9100.
- 14 G. K. Fu, G. N. Xu, S. P. Chen, L. Lei and M. L. Zhang, *Catal. Comm.*, 2013, **40**, 120-124.
- 15 S. Y. Wu, H. Zheng, Y. Y. Wu, W. Lin, T. Z. Xu and M. Guan, *Ceram. Int.*, 2014, **40**, 14613-14620.
- 16 Y. Q. Wang, X. F. Cheng, X. T. Meng, H. W. Feng, S. G. Yang and C. Sun, *J. Alloy Compd.*, 2015, **632**, 445-449.
- 17 J. Q. Zhang, K. Yu, Y. F. Yu, L. L. Lou, Z. Q. Yang, J. W. Yang and S. X. Liu, *J. Mol. Catal. A-Chem.*, 2014, **391**, 12-18.
- 18 X. F. Yang, H. Y. Cui, Y. Li, J. L. Qin, R. X. Zhang and H. Tang, *ACS Catal.*, 2013, **3**, 363-369.
- 19 Q. J. Xiang, D. Lang, T. T. Shen and F. Liu, *Appl. Catal. B-Environ.*, 2015, **162**, 196-203.
- 20 C. H. Xu, C. Wang, Y. H. Song, J. X. Zhu, Y. G. Xu, J. Yan, Y. X. Song and H. M. Li, *Chem. Eng. J.*, 2014, **241**, 35-42.
- 21 J. Y. Lei, Y. Chen, L. Z. Wang, Y. D. Liu and J. L. Zhang, *J. Mater. Sci.*, 2015, **50**, 3467-3476.
- 22 R. Yin, Q. Z. Luo, D. S. Wang, H. T. Sun, Y. Y. Li, X. Y. Li and J. An, *J. Mater. Sci.*, 2014, **49**, 6067-6073.
- 23 Y. M. He, Y. Wang, L. H. Zhang, B. T. Teng and M. H. Fan, *Appl. Catal. B-Environ.*, 2015, **168**, 1-8.
- 24 F. T. Li, Y. Zhao, Q. Wang, X. J. Wang, Y. J. Hao, R. H. Liu and D. S. Zhao, *J. Hazard. Mater.*, 2015, **283**, 371-381.
- 25 J. L. Zhao, Z. Y. Ji, X. P. Shen, H. Zhou and L. B. Ma, *Ceram. Int.*, 2015, **41**, 5600-5606.
- 26 M. Ou, Q. Zhong, S. L. Zhang and L. M. Yu, *J. Alloy Compd.*, 2015, **626**, 401-409.
- 27 H. Xu, Y. X. Song, Y. H. Song, J. X. Zhu, T. T. Zhu, C. B. Liu, D. X. Zhao, Q. Zhang and H. M. Li, *RSC Adv.*, 2014, **4**, 34539-34547.
- 28 H. F. Shi, C. L. Zhang and C. P. Zhou, *RSC Adv.*, 2015, **5**, 50146-50154.
- 29 H. P. Li, J. Y. Liu, W. G. Hou, N. Du, R. J. Zhang and X. Tao, *Appl. Catal. B-Environ.*, 2014, **160**, 89-97.
- 30 L. Y. Chen and W. D. Zhang, *Appl. Surf. Sci.*, 2014, **301**, 428-435.
- 31 F. J. Zhang, F. Z. Xie, S. F. Zhu, J. Liu, J. Zhang, S. F. Mei and W. Zhao, *Chem. Eng. J.*, 2013, **228**, 435-441.
- 32 S. Kumar, T. Surendar, A. Baruah and V. Shanker, *J. Mater. Chem. A*, 2013, **1**, 5333-5340.
- 33 H. Katsumata, T. Sakai, T. Suzuki and S. Kaneco, *Ind. Eng. Chem. Res.*, 2014, **53**, 8018-8025.
- 34 D. J. Martin, N. Umezawa, X. W. Chen, J. H. Ye and J. W. Tang, *Energy Environ. Sci.*, 2013, **6**, 3380-3386.
- 35 B. J. Zheng, X. Wang, C. Liu, K. Tan, Z. X. Xie and L. S. Zheng, *J. Mater. Chem. A*, 2013, **1**, 12635-12640.
- 36 L. Gu, J. Y. Wang, Z. J. Zou and X. J. Han, *J. Hazard Mater.*, 2014, **268**, 216-223.
- 37 X. Y. Guo, C. F. Chen, S. Y. Yin, L. J. Huang and W. P. Qin, *J. Alloy Compd.*, 2015, **619**, 293-297.
- 38 L. Q. Yea, J. Y. Liu, Z. Jiang, T. Y. Peng and L. Zan, *Appl. Catal. B-Environ.*, 2013, **142**, 1-7.
- 39 C. S. Pan, J. Xu, Y. J. Wang, D. Li and Y. F. Zhu, *Adv. Funct. Mater.*, 2012, **22**, 1518-1524.
- 40 Y. J. Wang, R. Shi, J. Lin and Y. F. Zhu, *Energy Environ. Sci.*, 2011, **4**, 2922-2929.
- 41 H. X. Zhao, H. T. Yu, X. Quan, S. Chen, Y. B. Zhang, H. M. Zhao and H. Wang, *Appl. Catal. B-Environ.*, 2014, **152**, 46-50.
- 42 J. Xu, W. L. Zhang, R. Shi and Y. F. Zhu, *J. Mater. Chem. A*, 2013, **1**, 14766-14772.
- 43 H. Katsumata, T. Hayashi, M. Taniguchi, T. Suzuki and S. Kaneco, *Mat. Sci. Semicon. Proc.*, 2014, **25**, 68-75.

- 44 S. B. Yang, Y. J. Gong, J. H. Zhang, L. Zhan, L. L. Ma, Z. Y. Fang, R. Vajtai, X. C. Wang and P. M. Ajayan, *Adv. Mater.*, 2013, **25**, 2452-2456.
- 45 Y. F. Wang, J. X. Liu, Y. W. Wang, C. M. Fan and G. Y. Ding, *Mat. Sci. Semicon. Proc.*, 2014, **25**, 330-336.
- 46 H. Y. Hu, Z. B. Jiao, H. C. Yu, G. X. Lu, J. H. Ye and Y. P. Bi, *J. Mater. Chem. A*, 2013, **1**, 2387-2390.
- 47 Y. F. Wang, X. L. Li, Y. W. Wang and C. M. Fan, *J. Solid State Chem.*, 2013, **202**, 51-56.
- 48 Z. H. Ai and S. C. Lee, *Appl. Surf. Sci.*, 2013, **280**, 354-359.
- 49 C. L. Bianchi, C. Pirola, E. Selli and S. Biella, *J. Hazard Mater.*, 2012, **211**, 203-207.
- 50 Y. X. Yang, W. Guo, Y. N. Guo, Y. H. Zhao, X. Yuan and Y. H. Guo, *J. Hazard Mater.*, 2014, **271**, 150-159.